

# Neural network reconstruction of the dense matter equation of state from neutron star observables

Shriya Soma<sup>a,b,c</sup> Lingxiao Wang<sup>a,c</sup> Shuzhe Shi<sup>d,e</sup> Horst Stöcker<sup>a,b,f</sup>  
Kai Zhou<sup>a,1</sup>

<sup>a</sup>Frankfurt Institute for Advanced Studies (FIAS), D-60438 Frankfurt am Main, Germany

<sup>b</sup>Institut für Theoretische Physik, Goethe Universität, D-60438 Frankfurt am Main, Germany

<sup>c</sup>Xidian-FIAS International Joint Research Center, D-60438 Frankfurt am Main, Germany

<sup>d</sup>Department of Physics, McGill University, Montreal, Quebec H3A 2T8, Canada.

<sup>e</sup>Center for Nuclear Theory, Department of Physics and Astronomy, Stony Brook University, Stony Brook, New York, 11794, USA.

<sup>f</sup>GSI Helmholtzzentrum für Schwerionenforschung GmbH, D-64291 Darmstadt, Germany

E-mail: [soma@fias.uni-frankfurt.de](mailto:soma@fias.uni-frankfurt.de), [lwang@fias.uni-frankfurt.de](mailto:lwang@fias.uni-frankfurt.de),  
[shuzhe.shi@stonybrook.edu](mailto:shuzhe.shi@stonybrook.edu), [stoecker@fias.uni-frankfurt.de](mailto:stoecker@fias.uni-frankfurt.de),  
[zhou@fias.uni-frankfurt.de](mailto:zhou@fias.uni-frankfurt.de)

**Abstract.** The Equation of State (EoS) of strongly interacting cold and hot ultra-dense QCD matter remains a major challenge in the field of nuclear astrophysics. With the advancements in measurements of neutron star masses, radii, and tidal deformabilities, from electromagnetic and gravitational wave observations, neutron stars play an important role in constraining the ultra-dense QCD matter EoS. In this work, we present a novel method that exploits deep learning techniques to reconstruct the neutron star EoS from mass-radius (M-R) observations. We employ neural networks (NNs) to represent the EoS in a model-independent way, within the range of  $\sim 1-7$  times the nuclear saturation density. The unsupervised Automatic Differentiation (AD) framework is implemented to optimize the EoS, so as to yield through TOV equations, an M-R curve that best fits the observations. We demonstrate that this method works by rebuilding the EoS on mock data, i.e., mass-radius pairs derived from a randomly generated polytropic EoS. The reconstructed EoS fits the mock data with reasonable accuracy, using just 11 mock M-R pairs observations, close to the current number of actual observations.

**Keywords:** Neutron Stars, Equation of States, Machine Learning

---

<sup>1</sup>Corresponding author.

---

## Contents

<b>1</b>	<b>Introduction</b>	<b>1</b>
<b>2</b>	<b>Reconstructing the EoS via Automatic Differentiation</b>	<b>3</b>
<b>3</b>	<b>TOV-Solver Network</b>	<b>4</b>
3.1	Piecewise Polyotropic Equations of State	5
3.2	TOV Equations: From EoS to Stellar Structure	6
3.3	Training the TOV-Solver Network	7
<b>4</b>	<b>EoS Network</b>	<b>8</b>
<b>5</b>	<b>Results and Discussion</b>	<b>10</b>
<b>6</b>	<b>Conclusions</b>	<b>15</b>
<b>7</b>	<b>Acknowledgements</b>	<b>15</b>
<b>A</b>	<b>TOV-Solver Network</b>	<b>20</b>
A.1	Fully Connected Dense Neural Network (FCN)	20
A.2	Convolutional Neural Network (CNN)	20
A.3	Long Short Term Memory (LSTM) Network	22
A.4	WaveNet	22
A.5	Comparison	22
<b>B</b>	<b>Mock Tests on SFHo and BHBA<math>\Lambda\phi</math> EoSs.</b>	<b>22</b>

---

## 1 Introduction

Neutron stars (NSs) harbour extreme conditions that are unattainable in terrestrial laboratories and are therefore instrumental in constraining the cold dense matter equation of state (EoS). The past decade has witnessed great progress in the research of these objects. NS observables like mass, radius, moment of inertia and tidal deformability are crucial in probing the EoS of strongly interacting dense matter. The mass measurements of pulsars have reached a high level of precision with observations via post-Keplerian parameters, e.g. Shapiro delay. Some of the most recent and accurate mass measurements include PSR J0348+0432, which has a mass of  $2.01 \pm 0.04 M_{\odot}$  [1], PSR J0740+6620, with a mass of  $2.08 \pm 0.07 M_{\odot}$  [2], and J1810+1714, with a mass of  $2.13 \pm 0.04 M_{\odot}$  [3]. The detection of gravitational waves from binary neutron star mergers (BNSMs) by the LIGO-Virgo collaboration has also made it possible to extract yet another parameter, the tidal deformability ( $\Lambda$ ), of excited neutron stars for the very first time. The analysis of the first BNSM collision event, GW170817, which was later accompanied by an electromagnetic counterpart, has led to an estimated value of,  $197 \leq \Lambda \leq 720$  [4, 5]. Furthermore, towards the end of 2019, NICER (Neutron Star Interior Composition Explorer) announced its first results on radius measurements of a pulsar, namely PSR J0030+0451 [6, 7]. With an expected substantial increase in observational data, it is possible to establish further constraints on the dense matter EoS. Experiments at

the GSI Helmholtzzentrum für Schwerionenforschung and the future Facility for Antiproton and Ion Research (FAIR) in Europe pave the way to compress baryonic matter to high densities and pressures through nucleus-nucleus collisions. The temperatures in these collisions are however high [8]. We therefore resort to observational data from cold, long lived NSs, particularly masses and radii, to further this study.

It has been demonstrated in previous studies that there exists a one-to-one mapping from the mass-radius (M-R) relationship of neutron stars to the EoS [9]. This is realized by inverting the Tolman–Oppenheimer–Volkoff (TOV) equations [10, 11], which are numerically solved to obtain the structural properties of NSs from a given EoS. With sufficiently many NS observations, spread across the M-R space, one can, in this way, try to extrapolate the NS EoS to the data from finite nuclei at low densities, and to perturbative QCD calculations at asymptotically high densities. Theoretical models which can generate possible EoSs that attempt to describe the dense matter inside NSs incorporate different physical assumptions for the strongly interacting dense matter. Non-relativistic and relativistic model EoSs may include only purely nucleonic degrees of freedom, hybrid (hadrons and quarks) models, models with hyperons, models with kaon condensates and pure quark models [12–20]. These EoSs can be used to predict the global properties of NSs, which can then be confronted with observational data. This allows to constrain NS parameters like maximum mass, radius, and tidal deformability, which are all dependent on the EoS [5, 21–24]. This method is however strongly model-dependent. It does not systematically translate existing NS observations to dense matter properties. Alternatively, EoSs are parameterized with piecewise polytropes [25, 26], spectral representations [27], or Gaussian processes [28, 29].

Previous attempts to reconstruct the EoS from M-R relations in a hopefully model-independent way, for example, rely on the well-known Bayesian inference. This approach utilizes a certain parameterization for the EoSs and applies particular choices for their priors [30–32]. One possible way to exploit directly the non-linear mapping between an M-R curve and its EoS, is the machine learning inference in the sense of supervised learning. Recent studies based on this strategy include works by Fujimoto et al. [33–35], Morawski et al. [36], Ferreira and Providência [37], and Krastev [38]. Fujimoto et al. developed a feed forward neural network which outputs the EoS in its speed of sound representation, when supplied with M-R observations. Morawski et al. used the encoder-decoder structure of the Auto-Encoder to reconstruct the EoS, without using any parametric representation. Ferreira and Providência used Support Vector Machines to regress the EoS in terms of nuclear matter parameters. Krastev showed that, from observational NS data, a trained feed forward neural network is capable of extracting the density dependence of the nuclear symmetry energy and therefore the EoS. In the present study, a model-independent reconstruction of the dense matter EoS is accomplished with statistical inference from M-R observations in an unbiased manner. The method introduced here utilizes deep neural networks (DNNs) in the Automatic Differentiation (AD) framework to reconstruct the NS EoS. This is the first implementation of an unsupervised learning algorithm for the EoS reconstruction. Additionally, the design of our inverse problem necessitates a functional form of the TOV equations that is easily differentiable. For this purpose, we train a DNN to solve the TOV equations, essentially modeling a **TOV-Solver Network**. The framework is tested on mock data generated using piece-wise polytropes for the EoS.

The layout of the article is as follows: Section 2 outlines the paradigm of Automatic Differentiation with DNNs in the reconstruction procedure of the NS EoS. Section 3 provides a description of the **TOV-Solver Network** and, accordingly, the data preparation process.

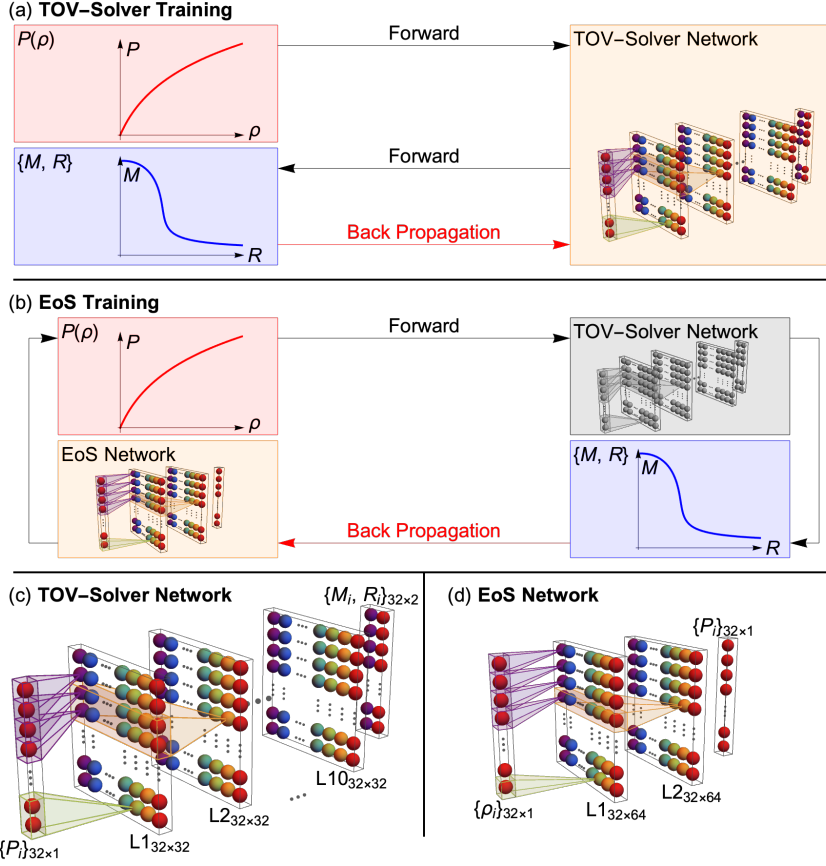


**Figure 1.** A flow chart of our methods, with TOV-Solver training (a) and EoS training (b). Note that in (b) the TOV-Solver Network is well-trained and frozen. The structure of the TOV-Solver Network and EoS Network are depicted in (c) and (d) respectively, in which, the colored spheres are nodes of the network, and the colors label the indices across the width in each layer. The shadow lines link the nodes between layers, and represent a 1D convolutional kernel operation with trainable parameters.

Section 4 details the specifics of the EoS Network and its optimization. The results are discussed in Section 5 and the conclusions are drawn in Section 6.

## 2 Reconstructing the EoS via Automatic Differentiation

Due to their abilities to capture complex nonlinear correlations in data, deep learning techniques have been proven useful in solving a number of physical problems, e.g. determining the parton distribution function [39, 40], reconstructing the spectral function [41–43], identifying phase transitions [44–49], assisting lattice field theory calculations [50–53], evaluating centrality distributions for heavy ion collisions [54–56], parameter estimation under detector effects [57, 58], and speeding up hydrodynamic simulations [59]. Earlier works that incorporated DL methods have shown that DNNs can potentially surpass traditional methods in solving inverse design problems [60–62]. In the course of this work, we explore the DNNs’

capacities to invert the TOV equations, in order to reconstruct the NS EoS from a limited set of M-R observations, through an unsupervised Automatic Differentiation framework.

Figure 1 summarizes the flow chart of our approach: Part(a) of figure 1 illustrates a primary DNN that is trained, supervised, to emulate the numerical methods used to solve the TOV equations, i.e. mapping a given EoS to its corresponding M-R curve, hence the name **TOV-Solver Network**<sup>1</sup>. Once trained, the network model is saved as a mapping from  $x$  to  $\mathbf{z}$ , where  $\mathbf{z} = f(x)$ . Here,  $x = P_i(\rho_i)$  is the pressure at fixed mass densities, which is the input to the **TOV-Solver Network**. The output,  $\mathbf{z} = (M_i, R_i)$ , represents the mass-radius pairs. The network model is composed of a series of differentiable modules which includes both linear transformations and nonlinear activation functions. In Figure 1(b), we inherit the well-trained **TOV-Solver Network** from the previous step with all its differentiable parameters frozen in subsequent procedures. A secondary DNN, the **EoS Network**, is introduced to represent the EoS in an unbiased and flexible manner, i.e.  $P_\theta(\rho)$ , where  $\{\theta\}$  is a set containing all parameters of the **EoS Network**. By coupling to the well-trained **TOV-Solver Network**, the **EoS Network** is optimized in an unsupervised manner to fit the combined output to the M-R observations. Hence, given the number of M-R observations,  $N_{\text{obs}}$ , the loss function for training is the standard  $\chi^2$  between the observations and the predictions of the pipeline “**EoS Network**  $\rightarrow$  **TOV-Solver Network**”, and is given by

$$\chi^2 = \sum_{i=1}^{N_{\text{obs}}} \frac{(M_i - M_{\text{obs},i})^2}{\Delta M_i^2} + \frac{(R_i - R_{\text{obs},i})^2}{\Delta R_i^2}. \quad (2.1)$$

Here,  $(M_i, R_i)$  is the predicted output of the observation  $(M_{\text{obs},i}, R_{\text{obs},i})$ , which has an uncertainty  $(\Delta M_i, \Delta R_i)$ . Given a frozen **TOV-Solver Network**, we can derive the gradients of its parameters as

$$\frac{\delta \chi^2}{\delta \theta} = \frac{\delta \chi^2}{\delta \mathbf{z}} \frac{\delta \mathbf{z}}{\delta P_\theta} \frac{\delta P_\theta}{\delta \theta}. \quad (2.2)$$

Here, the last two terms can be directly computed using a back-propagation algorithm [63] within the AD framework for the two coupled DNNs. In other words, we are essentially fine-tuning the parameters of the **EoS Network** to obtain the desired M-R curve, after going through the frozen **TOV-Solver Network**, with guidance from a limited set of observational data. The architectures of the **TOV-Solver Network** and the **EoS Network** are shown in Figure 1 as part (c) and (d), respectively. We utilized the Python Library Keras [64], which is built on the Tensorflow platform [65], to setup the network models and to perform the AD calculations for optimizing the NS EoS.

### 3 TOV-Solver Network

This section describes the **TOV-Solver Network** devised for the present work. The network is built on a supervised learning scheme with the purpose of efficiently solving the TOV equations, i.e. to obtain the M-R curve from an arbitrary EoS. We therefore set the EoSs as the input to the network and train the network to output the corresponding M-R sequences. The training and validation of the **TOV-Solver Network** demands sufficient data. In the following subsections, we provide information on the data-generation process implemented in our study. Subsection 3.1 is devoted to the preparation of polytropic EoSs, subsection 3.2 to

<sup>1</sup>The universal approximation theorem ensures that DNNs can approximate any kind of continuous function with nonlinear activation functions [63].

the TOV equations and their solutions, and subsection 3.3 to the training of the TOV-Solver Network and subsequent investigation of its performance.

### 3.1 Piecewise Polyotropic Equations of State

A multitude of equations of state (EoSs) is generated spanning wide ranges in the pressure-density ( $P - \rho$ ) plane. This is achieved by parameterizing the EoSs in terms of piecewise polytropes. The low-density part of each EoS ( $\rho < \rho_{\text{sat}}$ , where  $\rho_{\text{sat}} \sim 2 \times 10^{14} \text{ g cm}^{-3}$  is the nuclear saturation density) is assumed to conform to a conventional nuclear EoS. Nevertheless, in order to introduce robustness in the training dataset, the low-density regime of the EoSs in the present study is assumed to comply with one of SLy [66], PS [67] or DD2 [68] EoSs. For the high-density region ( $\rho > \rho_{\text{sat}}$ ), we adopt the density segmentation scheme from Ref [26], i.e. any EoS can be reasonably well parameterized with five polytropic segments. The high-density region of the EoSs is chosen within the range  $[\rho_{\text{sat}}, 7.4\rho_{\text{sat}}]$ . This upper limit follows from the evidence that the pressure at this density,  $P(\rho = 7.4\rho_{\text{sat}})$ , affects the maximum mass of the neutron star [69]. The density is uniformly spaced on a logarithmic scale. The five segments are separated at densities (1.0, 1.4, 2.2, 3.3, 4.9, 7.4)  $\rho_{\text{sat}}$ , as in Ref. [26]. The pressure in the  $i^{\text{th}}$  segment is given as a function of the density  $\rho$ ,

$$P = K_i \rho^{\Gamma_i} \quad \text{for } i = [1,5], \quad (3.1)$$

where,

- (i)  $\rho \in [\rho_{i-1}, \rho_i]$ , with  $\rho_{i-1}$  and  $\rho_i$  being the minimum and maximum densities of segment  $i$ .
- (ii)  $K_i = P_{i-1} / \rho_{i-1}^{\Gamma_i}$ .
- (iii) Following Ref. [26], the adiabatic index,  $\Gamma_i$  is assigned random values in the range  $[1, \min\{5, \Gamma_{\text{luminal}}\})$ , where  $\Gamma_{\text{luminal}}$  sets the limit for the causal condition, i.e. the speed of sound,  $c_s$ , does not exceed the speed of light,  $c$ . Hence,  $c_s = \sqrt{dP/d\epsilon} < 1$ , or

$$\Gamma \equiv \Gamma_{\text{luminal}} \quad \text{when} \quad \frac{dP}{d\epsilon} = 1. \quad (3.2)$$

Here,  $\epsilon$  is the energy density, given by

$$\epsilon = \left( \frac{\epsilon(\rho_{i-1})}{\rho_{i-1}} - \frac{P_{i-1}}{(\Gamma_i - 1)\rho_{i-1}} \right) \rho + \frac{K_i}{\Gamma_i - 1} \rho^{\Gamma_i}, \quad (3.3)$$

for  $\Gamma \neq 1$ , and

$$\epsilon = \frac{\epsilon(\rho_{i-1})}{\rho_{i-1}} \rho + K_i \ln \left( \frac{1}{\rho_{i-1}} \right) \rho - K_i \ln \left( \frac{1}{\rho} \right) \rho, \quad (3.4)$$

for  $\Gamma = 1$  (see Ref. [26] or [69] for details).

With this prescription, three sets of 100,000 polytropic EoSs for each category, SLy, PS and DD2, are generated. A few of the generated EoSs are depicted in Figure 2.

### 3.2 TOV Equations: From EoS to Stellar Structure

The Tolman–Oppenheimer–Volkoff (TOV) equations are derived from the Einstein equations for a spherically symmetric star in hydrostatic equilibrium [10, 11]. They are given as

$$-\frac{dP}{dr} = \frac{[\epsilon(r) + P(r)][m(r) + 4\pi r^3 P(r)]}{r[r - 2m(r)]}, \quad (3.5)$$

and

$$\frac{dm(r)}{dr} = 4\pi r^2 \epsilon(r). \quad (3.6)$$

Here,  $r$  is the radial distance from the centre of the star, and  $m(r)$  is the mass enclosed within the radial distance,  $r$ . In order to determine the observables, mass ( $M$ ) and radius ( $R$ ) of the star, the TOV equations are integrated radially outwards from the centre. The initial conditions taken at the centre of the star are,  $r = 0$ ,  $m(r = 0) = 0$ ,  $\epsilon(r = 0) \neq 0$ ,  $P(r = 0) = P_c$ , where  $P_c$  is the central pressure, obtained from the EoS, usually given as a table. The radius,  $R$ , of the star is defined by the vanishing pressure condition at the surface ( $P(r = R) = 0$ ), and the mass enclosed in  $R$  is the total mass of the star, i.e.  $M = m(R)$ . Thus, the mass-radius (M-R) sequences are calculated for all the EoSs generated in subsection 3.1, a few of which are depicted in Figure 3 (corresponding to the EoSs in Figure 2). From this set of data, we exclude all the EoSs (and their corresponding M-R sequences) which fail to accommodate a neutron star of mass  $1.9M_\odot$ . This preference of a conservative limit follows from the observations [1, 2, 70], and leaves us with 94,462 EoSs corresponding to PS; 61,273 EoSs corresponding to SLy; and 72,834 EoSs corresponding to DD2 for training and validating the TOV-Solver Network.

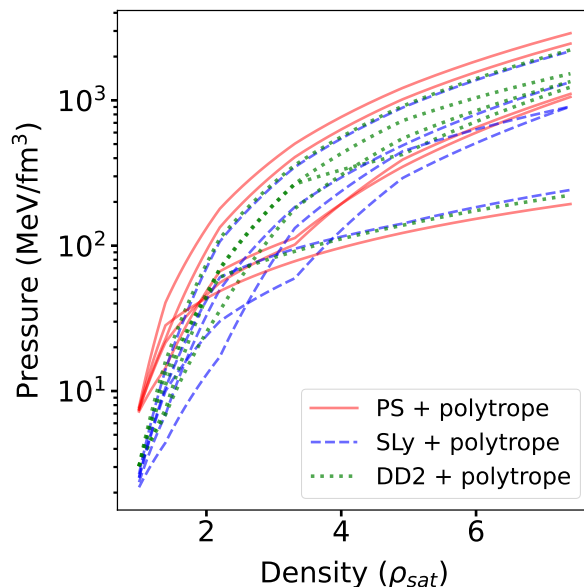


**Figure 2.** A few piece-wise polytropic EoSs that were generated using PS (red), SLy (blue) or DD2 (green) EoSs for the low-density region. A major portion of the pressure range is spanned by the EoSs.



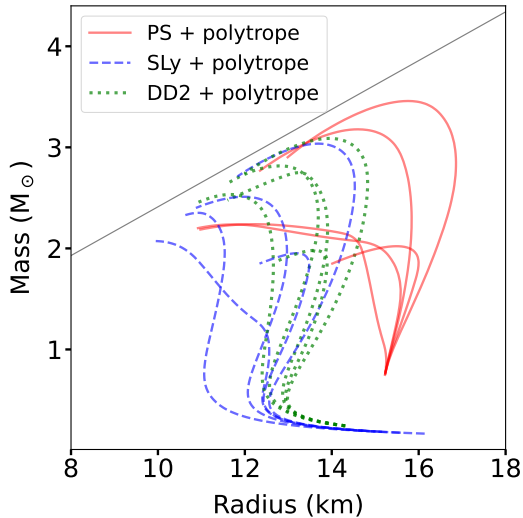


**Figure 3.** The Mass-Radius curves correspond to the EoSs plotted in Figure 2, obtained by solving the TOV equations. The gray line denotes the causal limit.

### 3.3 Training the TOV-Solver Network

The simulated data from subsections 3.1 and 3.2 are used to train the **TOV-Solver Network**. The deep learning model, WaveNet, is adopted to perform this emulator task. WaveNet is a generative neural network model with autoregressive properties. It mimics the concept of autoregression which is exercised in solving the TOV equations (see subsection 3.2). Therefore, it is used here to resemble the conventional numerical methods. The EoSs which are input to the **TOV-Solver Network** are represented in a discretized format,  $P_i \equiv P(\rho_i)$ . The contribution to the EoSs from the low density region ( $\rho < \rho_{sat}$ ) are omitted in the network as these values have been established in our work to follow one of the three conventional nuclear EoSs: PS, SLy or DD2. Thus, we designate the input layer as  $P_i \equiv P(\rho_{sat} \leq \rho_i \leq 7.4\rho_{sat})$ , a single channel, i.e, an array of pressure, with shape  $(N_\rho, 1)$ , where  $N_\rho$  is the number of discrete density values. The output however has a shape  $(N_\rho, 2)$ , i.e, two channels for the mass  $M$ , and radius,  $R$ , respectively. Two different resolutions for the EoS representation are used here, namely  $N_\rho = 128$  or  $32$ . It is realized in subsequent assessments that a coarse resolution suffices to accomplish the desired results. The model uses logarithmic values of pressure as the input. Both the input and the output arrays are normalized to constitute elements that lie within the range  $(0,1)$ . Additional information on the network design and training is supplied in Appendix A <sup>2</sup>. Figure 4 shows that the trained **TOV-Solver Network** is successful in capturing the mapping of randomly given EoSs to the corresponding M-R curves. Note that the trained **TOV-Solver Network** also works well on SFHo and BHBA $\phi$  EoSs as shown in Figure 4. The M-R curves are successfully reproduced by the DL models to a very high precision, with the coefficient of determination  $\mathcal{R}^2 \sim 99.9\%$ . This illustrates that DNNs have the capacity to replace conventional numerical methods used for solving the TOV

<sup>2</sup>A few additional DL models, namely, the fully connected neural network (FCN), Convolutional neural network (CNN), and Long Short Term Memory (LSTM), were also evaluated based on their execution of this task. Appendix A entails a description of their structures and an analysis of their performances.



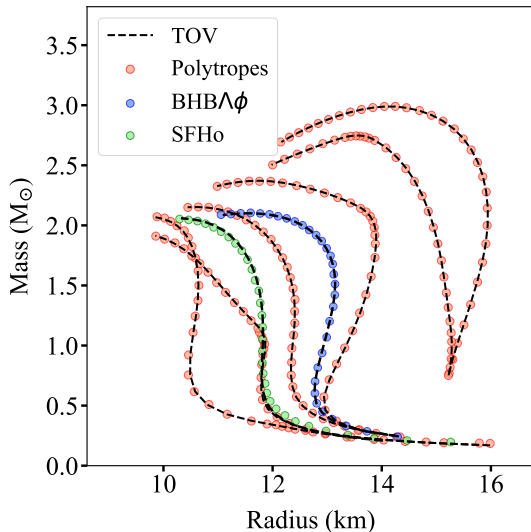


**Figure 4.** The TOV-Solver Network predictions using the WaveNet model for several unseen test EoSs are shown against the ground truth values of the M-R curves. The dashed black line is output from TOV equations and the markers denote the network predictions. The blue and green dotted M-R curves represent the network predictions for BHBA $\phi$  and SFHo EoSs respectively.

equations. In comparison to numerical calculations like the Euler or Runge-Kutta methods, the network emulator used here, is (i) superior in computational efficiency, ( $\sim 10^6$  sec faster), and (ii) easily differentiable. This is critical for applying back-propagation in the AD framework, deployed in the following section for statistical inference of the EoS reconstruction. The trained TOV-Solver Network model and weights are saved.

## 4 EoS Network

The EoS Network is introduced into the pipeline at this stage (see Figure 1(b)). It is modeled with density,  $\rho$ , as input and the corresponding pressure,  $P_\theta(\rho)$ , as output. The EoS output ( $P_\theta(\rho)$ ) from the EoS Network is further input to the well-trained TOV-Solver Network, thus linking the two networks. The TOV-Solver Network parameters are set as non-trainable weights prior to the EoS optimization process. The trainable weights of the EoS Network are then optimized in this pipeline to fit the predicted M-R output to mock observational data, thereby inverting the TOV equations. Compared to earlier studies which captured the inverse mapping from M-R observations to the EoS [33–38], the proposed method belongs to the unsupervised learning paradigm, which can be cast as a generalized Bayesian inference, with augmentations in the following aspects: (i) the EoS is represented in an unbiased manner as a DNN, thus the parameters to optimize are the network weights and biases; (ii) the traditional numerical methods to solve the TOV equations are replaced by a well-trained TOV-Solver network, thus simplifying and speeding up the following AD process; and (iii) the optimization uses a gradient-descent based approach within the AD framework as depicted in Figure 1(b). The network architecture and the optimization procedure are given below.

The input density to our pipeline is a linearly spaced 1D array of length  $N_\rho = 32$ , normalized to lie within (0,0.1). The trained WaveNet model of the same resolution is deployed as the **TOV-Solver Network**<sup>3</sup>. The **EoS Network** architecture utilizes three 1D convolutional layers (two hidden layers, and one output layer) as depicted in Figure 1(d). The hidden layers have 64 feature maps each. A kernel of size  $1 \times 1$  is used, with the kernel weights initialized from a *He* normal distribution [71]. The  $L_2$  regularizer,  $\lambda = 10^{-8}$ , is exercised on the weights, and the *same* padding is applied to all layers. The Sigmoid activation function is used on the output layer, and the ELU activation function on the hidden layers. By using kernel size  $1 \times 1$ , we ensure that each input element shares the same parameters in the above architecture. Therefore, the induced relationship between the  $i^{\text{th}}$  input density neuron,  $\rho_i$ , and corresponding output pressure,  $P_i$ , is equivalent to a fully connected DNN representation with two hidden layers consisting of 64 neurons each. Thus, the **EoS Network** uses a total of 4353 parameters for defining  $P_\theta(\rho)$ . We further specify the weights of each layer in the **EoS Network** to be non-negative. This preserves the order of the input layer up to the output layer,  $P(\rho)$ . Thus, we establish monotonicity in the represented function  $P(\rho)$ , a condition that is required by any physical EoSs. This method also ensures that the reconstructed EoS is a well correlated function. Contrary to the general use of large datasets in training a neural network, the optimization procedure in our approach requires just one M-R sequence. Each training epoch therefore has a batch size 1, i.e, in the ideal situation, we are required to only optimize the unique dense matter EoS to fit M-R observations. However, we adapt to the realistic scenario where all observational data comes with sizeable uncertainties (further details in Section 5).

Assuming  $N_{\text{obs}}$  is the number of reliable M-R observations, the loss function for the training is given by Eq. (2.1). It is defined as the distance between the observations and the M-R curve as predicted from the network pipeline above, i.e. the likelihood of observations given an EoS and its corresponding M-R curve from the **TOV-Solver Network**. However, the observational data is not spread uniformly across the M-R space, and the measurement uncertainties are likely to cause discontinuities in the M-R curve. Furthermore, the data is limited and the central density, ( $\rho_{ci}$ ), to which an uncertain observation corresponds to, is unknown. In other words, the  $i^{\text{th}}$  M-R observation, ( $M_i, R_i$ ), does not necessarily correspond to the  $i^{\text{th}}$  central density,  $\rho_{ci}$ , in the input layer<sup>4</sup>. To evaluate the loss function optimally, we adopt the ‘closest approach’ method as implemented in Ref. [31]. Thus, within each iteration during the training, we evaluate the loss as

$$\chi^2 = \sum_{i=1}^{N_{\text{obs}}} \frac{(M(\rho_{ci}) - M_{\text{obs},i})^2}{\Delta M_i^2} + \frac{(R(\rho_{ci}) - R_{\text{obs},i})^2}{\Delta R_i^2}. \quad (4.1)$$

Here,  $\rho_{ci}$  for every  $i^{\text{th}}$  observation is updated as,

$$\rho_{ci} = \arg \min_{\rho_c} \frac{(M(\rho_c) - M_{\text{obs},i})^2}{\Delta M_i^2} + \frac{(R(\rho_c) - R_{\text{obs},i})^2}{\Delta R_i^2}. \quad (4.2)$$

Eq. (4.2) is therefore used to determine the central densities of ( $M_{\text{obs}}, R_{\text{obs}}$ ) that lead to the least distance between the M-R curve obtained from the **TOV-Solver Network** and the M-R observations. The Adam optimizer [72] was utilized here, with varying learning rates ( $\alpha$ 's)

<sup>3</sup>All the trained DL models were tested in the pipeline. Optimum results were obtained with the WaveNet and LSTM

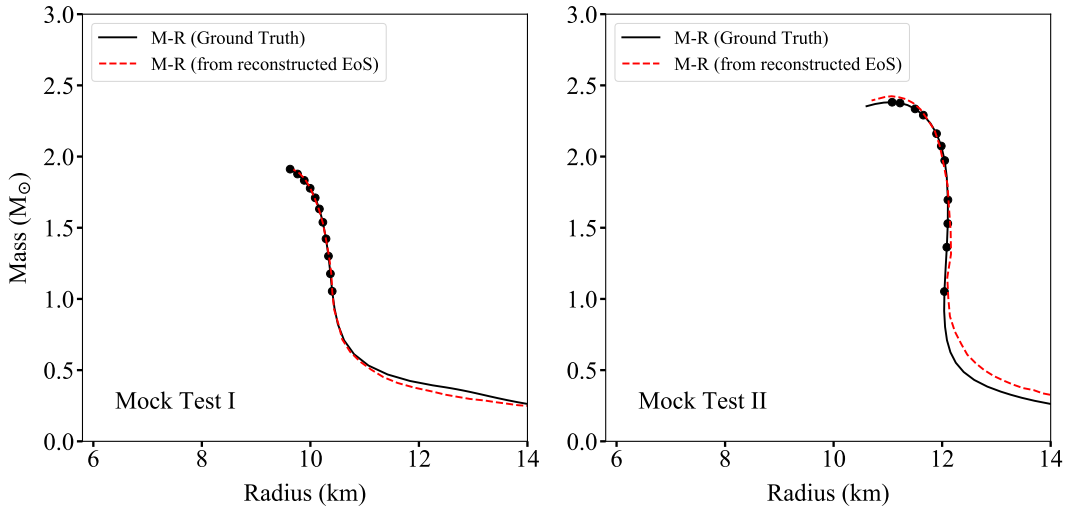
<sup>4</sup>In such circumstances, a finer resolution ( $N_\rho = 128$ ) might prove useful.

for different stages of the training process where smaller learning rates are usually used at later stages to stabilize the training. The learning progress of the network is moderated by decreasing the loss function  $\chi^2$ . The learning rate for one such reconstruction in the present study, is scheduled as follows: 1000 epochs ( $\alpha = 0.001$ ), 1000 epochs ( $\alpha = 0.005$ ), 1500 epochs ( $\alpha = 0.003$ ), 1600 epochs ( $\alpha = 0.0001$ ) and, finally, 2000 epochs ( $\alpha = 0.00003$ ), in the order specified. The reason for the small changes in the learning rates is that they have minor effects on the final results. Using this method, the EoS is reconstructed with an uncertainty which is proportional to the statistical uncertainty of the observations. In certain cases where the causal condition is not fulfilled, the DNN fails to produce a realistic EoS. This is also seen from the lack of convergence of the loss during the optimization process. This issue is resolved by applying the causal condition to reject those EoSs.

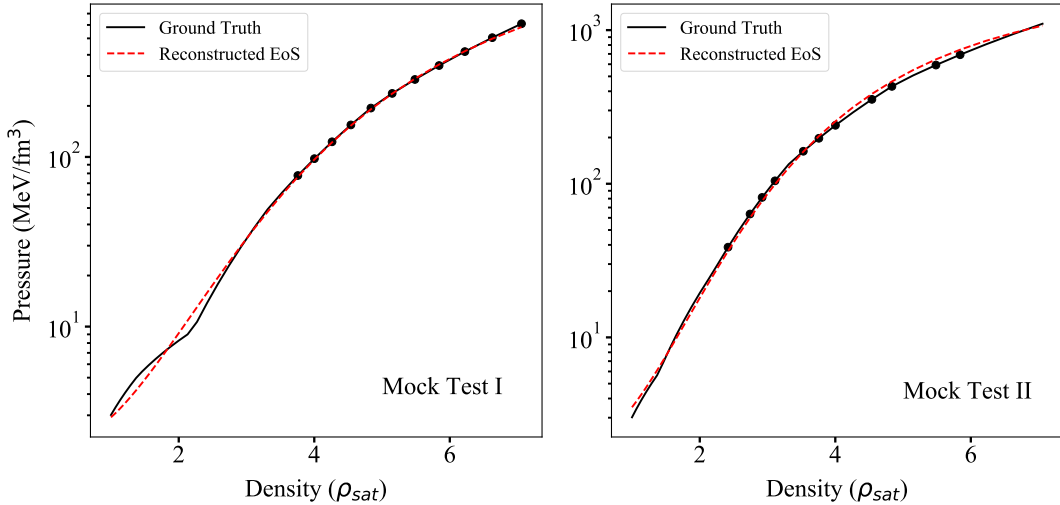
## 5 Results and Discussion

The reconstruction method proposed here is examined by closure tests that are first performed in an ideal case of mock data, i.e, synthetic M-R mock data without systematic and statistical uncertainties. We use two sets of such mock data from M-R curves which correspond to two randomly chosen EoSs as depicted in Figure 6. The black solid lines in the figures are the targets for the reconstruction attempt. The absence of low mass NSs ( $< 1M_\odot$ ) in nature compels us to use mock data with masses above  $1M_\odot$ . Figure 5 depicts two sets of such mock observations each containing 11 M-R points, which are chosen from the region  $M > 1M_\odot$  along the M-R curve. These 11 highlighted black points lie on the M-R curve (ground truth). With our proposed method, the EoSs from these two sets of mock M-R data are reconstructed. Figure 6 displays a comparison of the EoS reconstructed by the DNN in this work (dashed red line) with the ground truth (solid black line). Evidently, the reconstruction of the EoSs is fairly successful in the range  $M > 1M_\odot$  for the ideal scenarios. The reconstruction of the EoSs by the DNN is remarkably close to the ground truth in the high-density region (i.e., corresponding to the high mass region in M-R curve). The deviation of the reconstructed EoSs from the ground truth in the low-density regime is attributed to the lack of mock data below  $1M_\odot$ . This is also demonstrated in Figure 6, where the 11 black solid points on the EoSs correspond to the 11 mock data points on the M-R curves in Figure 5. The red dashed curves in Figure 5 are the M-R curves corresponding to the reconstructed EoSs as predicted by the TOV-Solver Network. The two M-R curves agree with each other reasonably well. For a sanity check, one can obtain the M-R curve of the reconstructed EoS by directly solving the TOV equations and compare the respective results.

We proceed to the realistic situation where the observations inevitably involve uncertainties. The proposed method is tested on the same mock M-R data as in Figure 5, albeit with uncertainties included. To incorporate statistical noise, for each of the two mock tests, multiple M-R curves are sampled from a normal distribution around the true M-R values,  $\mathcal{N}(M_i; R_i; \sigma_{M_i}; \sigma_{R_i})$ . A 10% relative standard deviation is assigned to each mass and radius, i.e  $\Delta M_i = 0.1M_i$  and  $\Delta R_i = 0.1R_i$ . Therefore, 500 mock M-R data samples are drawn from a normal distribution with  $\sigma_M = 0.1M$ ,  $\sigma_R = 0.1R$ . In Figure 7, the true M-R curves are represented by the black solid line and the highlighted circles mark the 11 M-R mock data, which are the mean values of the respective normal distributions. The blue point-cloud in Figure 7 depicts all 500 sampled sets of the mock data points resulting from the true M-R curve, where each sampled set contains just 11 M-R pairs, all above  $\sim 1M_\odot$ , to be consistent with the current real observations. The optimization procedure is repeated for



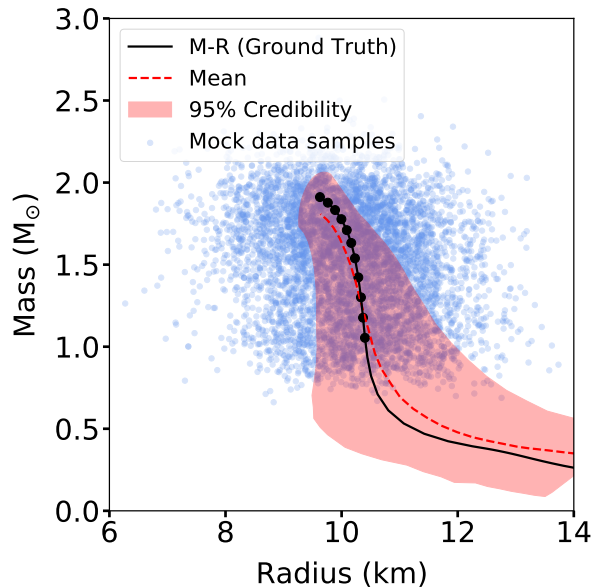
**Figure 5.** The 11 M-R mock data (black points) located in the region  $M > 1M_{\odot}$  along the ground truth M-R curve (black solid line). A reasonable agreement of the M-R curve from the reconstructed EoS (red dashed line) with the ground truth curve is depicted in the mass region  $M > 1M_{\odot}$ . The left and right panels respectively represent the Mock Test I and Mock Test II.



**Figure 6.** The comparison of the EoS reconstructed by our method (dashed red line) and the ground truth (solid black line). The black points shown, when taken as central densities for the NSs, correspond to the mock M-R “observations” in Figure 5. The left and right panels respectively represent the Mock Test I and Mock Test II.

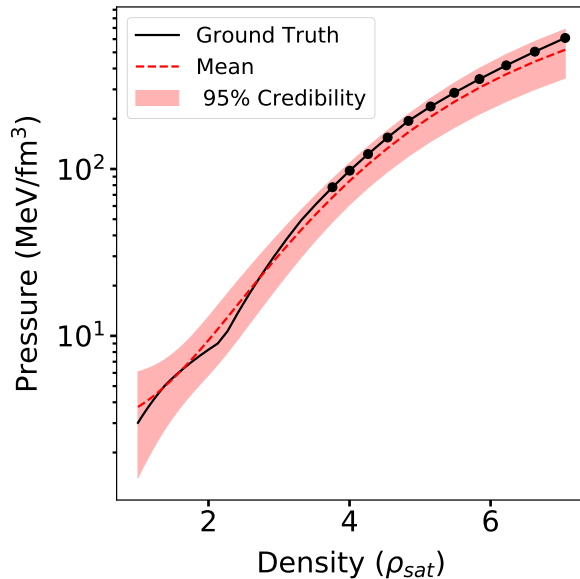
the 500 samples and the results are shown in Figure 8. For each sampled set of mock data, the proposed method reconstructs exactly one EoS in the sense of maximum a posteriori probability (MAP). In this closure test, the uncertainty of the reconstruction is evaluated

by fitting the reconstructed EoSs to a uni-variate normal distribution,  $\mathcal{N}(\mu_i, \sigma_i)$ . This is straightforward and a  $2\sigma$ , 95% confidence level of the reconstructed, model-independent EoS is shown in Figure 8 as the shaded region. The dashed red curve in the shaded region is the mean value of the reconstructed EoSs. The **TOV-Solver Network** predicts the M-R curves corresponding to each of the reconstructed EoSs. The M-R predictions of the **TOV-Solver Network** from the reconstructed EoSs are then subjected to a normal distribution fit. In this case, all M-R points with the same central density  $\rho_{c,i}$  (i.e. the ensemble of each element from the output sequence) are fitted with a separate bi-variate Gaussian distribution, given by  $p((M_i, R_i)|P_j) = \mathcal{N}(\mu_i, \sigma_i)$ . The 95% confidence level is determined from the  $2.44\sigma_i$  interval for 2D distributions. This uncertainty band of the M-R curve is depicted by the orange band in Figure 7. The resulting mean M-R curve from the bi-variate distribution is represented by the dashed red line. When compared to the uncertainty of the mock M-R data samples (blue point clouds), it is evident that the width of the M-R curves obtained from the reconstructed EoSs is considerably smaller. This illustrates the potential of the present novel EoS reconstruction method - it works despite the large uncertainties in the mock M-R data. For a few sample M-R curves, the NN fails to produce a realistic EoS. The causal condition is applied to filter out these EoSs which fail to converge. In certain cases, a failure can also be ascribed to the large uncertainties of individual M-R pairs which leads to outliers of the M-R curve. Moreover, the points on the M-R curve are assumed to fall in the ascending order of their mean mass. However, accounting for large uncertainties while sampling from a Gaussian distribution, may result in a disordering of the M-R pairs.



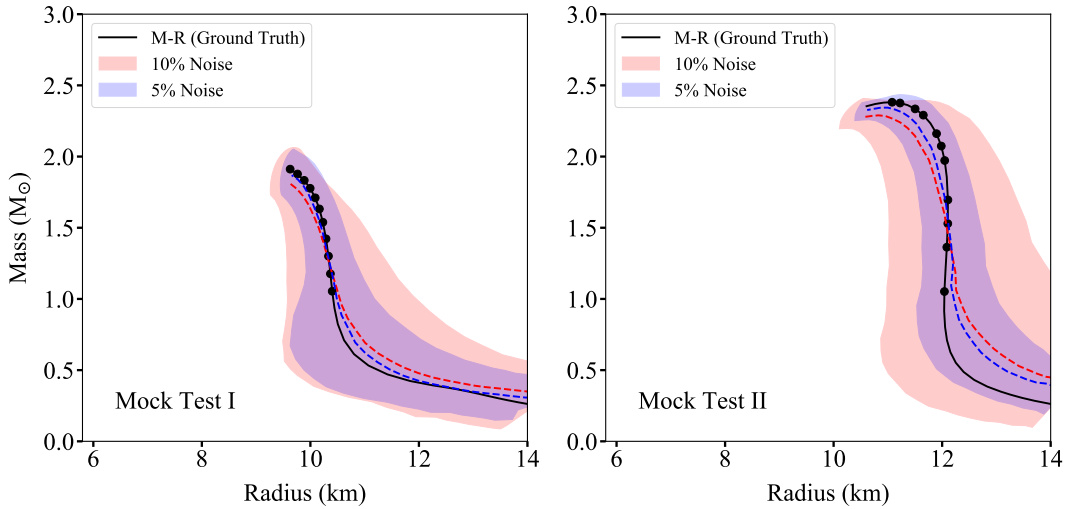
**Figure 7.** The blue point cloud represents the M-R mock data ensembles w.r.t mock test I, sampled with 10% uncertainties from the ground truth M-R curve (black solid line). The 95% confidence level of the M-R band from the reconstructed EoSs is depicted as the orange shaded region, and the mean as a red dashed line.

Figure 9 and 10 show the performance of the EoS reconstruction for both mock test



**Figure 8.** Comparison of the ground-truth (black solid line) and the reconstructed EoS (red dashed line) with uncertainty (orange band) by using M-R mock data from Figure 7.

I and II when different observational uncertainties are assumed: the relative noise level of mock data are set to 10% and 5% of the “observed” mean. The systematic error can, in this case, be quantified from both the uncertainty of the *TOV-Solver Network*, and of the *EoS Network*. The results shown in Figure 10 demonstrate that the mean of the reconstructed EoSs is closer to the ground truth in the case with 5% error as compared to the case with 10% error. The uncertainty band narrows down with decreasing error. Hence, the availability of precise future observations can provide great scope for the reconstruction of a better constrained EoS using the present method. The closure tests above demonstrate that the present AD based method with DNNs reliably reconstructs the underlying dense NS matter EoS, given limited NS M-R observations, with substantial measurement errors. This method applies an unbiased representation for the EoS with DNNs, and thus introduces an unique model-independence into the exploration of the properties of dense matter from NS structural observations. While Bayesian approaches can use polytropic EoSs for a model-independent reconstruction, the optimization in a multi-dimensional parameter space is computationally inefficient. Moreover, as the AD framework uses a pre-trained DNN to emulate the TOV equations, the method proposed here is fast and efficient. When compared to supervised learning approaches on the same problem, the present new method possesses a natural Bayesian picture for its interpretation and for estimating the uncertainties related to the observational noise, besides providing a novel alternative for the EoS reconstruction. This work can be further extended to incorporate a Bayesian Neural Network. An interesting aspect which can be explored is the inclusion of EoSs which undergo a first-order phase transition (FOPT) or a crossover from hadronic matter to quark matter. There is a possibility of such an occurrence of a FOPT in the cores of NSs, which may have dramatic consequences also for binary neutron star mergers, BNSMs [73], and for core collapse supernovae. In the



**Figure 9.** The ground truth M-R curve (black solid line) and the M-R relationship from reconstructed EoSs with mean (red dashed line for 10% noise level, blue for 5%) and uncertainty (orange band for 10% noise level and blue for 5%) depicted. The left and right panels respectively represent the Mock Test I and Mock Test II.

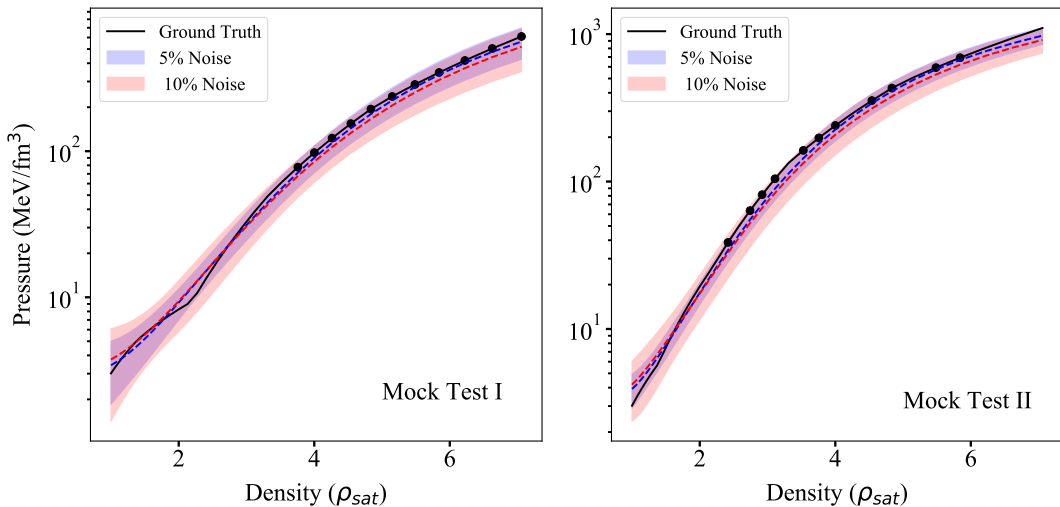


**Figure 10.** The EoS reconstruction under different levels of uncertainties on the M-R mock observations, with the blue band denoting a 5% noise level and the orange band denoting a 10% noise level. The corresponding dashed lines represent the respective mean of the reconstructed EoSs. The left and right panels respectively represent the Mock Test I and Mock Test II.

current study we do not include such EoSs (e.g., constant pressure with increasing energy density) in the data-set.

A similar study can also be carried out by using the M- $\Lambda$  relationships of NSs. The tidal



deformability estimates obtained from GWs however, have even larger uncertainties. Future measurements from next generation GW detectors, like LIGO India, KAGRA, Einstein Telescope, Cosmic Explorer and LISA, with greater sensitivities will yield better constrained estimates for tidal deformability. The present study is restricted to M-R observations of long-lived cold neutron stars, and tested on synthetic mock data (investigation based on real data is in progress). The study can be further extended to observations from proto-neutron stars and to remnants of BNSMs, where the high temperatures cannot be ignored. The thermal contributions in the pressure can be incorporated separately in a piecewise polytropic approach, such as,  $P = P_{\text{cold}} + P_{\text{thermal}}$ . The adiabatic index of the thermal pressure has been examined in earlier works and can be set to  $\Gamma_{\text{th}} \sim 1.5\text{-}2.0$  [74]. With an increase in the number of GW event detections, there is future scope for the study of long-lived remnants from BNSMs using a non-zero temperature EoS.

## 6 Conclusions

This work introduces a novel Automatic Differentiation (AD)-based approach with DNNs to reconstruct the EoS from stellar observations. In a Bayesian inference picture, the EoS is represented by DNNs (**EoS Network**) without explicit physical model priors. In combination with the other supervised trained DNNs (**TOV-Solver Network**), which emulate the TOV equations solver, the AD is applied to reconstruct the EoS using a gradient-based optimization by fitting NS M-R mock data. We first train the **TOV-Solver Network** and show that it can successfully replace the numerical ODE solvers, in fact, in a more efficient and easily differentiable manner. Several closure tests with mock M-R data show that the proposed approach effectively reconstructs the underlying EoS and also evaluates the associated uncertainties. Furthermore, we demonstrate that a higher precision on future measurements of NS global properties with next-generation telescopes and detectors can provide the scope for a fine reconstruction of the EoS of NS matter. This also proves the reliability of the proposed method.

## 7 Acknowledgements

The authors thank Dr. Jan Steinheimer and Dr. Anton Motornenko for useful discussions. This work is supported by (i) Deutscher Akademischer Austauschdienst - DAAD, and GSI-F&E funds (S. Soma), (ii) BMBF under the ErUM-Data project (K. Zhou), (iii) the AI grant of SAMSON AG, Frankfurt (S. Soma, L. Wang and K. Zhou), (iv) Xidian-FIAS International Joint Research Center (L. Wang), (v) Natural Sciences and Engineering Research Council of Canada (S. Shi), (vi) Bourses d'excellence pour étudiants étrangers (PBEEE) from Le Fonds de Recherche du Québec - Nature et technologies (FRQNT) (S. Shi), (vii) U.S. Department of Energy, Office of Science, Office of Nuclear Physics, grant No. DE-FG88ER40388 (S. Shi), and (viii) Walter Greiner Gesellschaft zur Förderung der physikalischen Grundlagenforschung e.V. through the Judah M. Eisenberg Laureatus Chair at Goethe Universität Frankfurt am Main (H. Stöcker). We also thank the NVIDIA Corporation for donation of NVIDIA GPUs.

## References

- [1] J. Antoniadis, P.C.C. Freire, N. Wex et al., *A Massive Pulsar in a Compact Relativistic Binary*, *Science* **340** (2013) .

- [2] E. Fonseca, H.T. Cromartie, T.T. Pennucci, P.S. Ray, A.Y. Kirichenko, S.M. Ransom et al., *Refined mass and geometric measurements of the high-mass PSR j0740+6620*, *The Astrophysical Journal Letters* **915** (2021) L12.
- [3] R.W. Romani, D. Kandel, A.V. Filippenko, T.G. Brink and W. Zheng, *PSR j1810+1744: Companion darkening and a precise high neutron star mass*, *The Astrophysical Journal Letters* **908** (2021) L46.
- [4] M.W. Coughlin, T. Dietrich, Z. Doctor, D. Kasen, S. Coughlin, A. Jerkstrand et al., *Constraints on the neutron star equation of state from AT2017gfo using radiative transfer simulations*, *Monthly Notices of the Royal Astronomical Society* **480** (2018) 3871.
- [5] LIGO SCIENTIFIC COLLABORATION AND VIRGO COLLABORATION collaboration, *Properties of the binary neutron star merger gw170817*, *Phys. Rev. X* **9** (2019) 011001.
- [6] T.E. Riley, A.L. Watts, S. Bogdanov, P.S. Ray, R.M. Ludlam, S. Guillot et al., *A NICER View of PSR J0030+0451: Millisecond Pulsar Parameter Estimation*, *ApJL* **887** (2019) L21.
- [7] M.C. Miller, F.K. Lamb, A.J. Dittmann, S. Bogdanov et al., *PSR J0030+0451 Mass and Radius from NICER Data and Implications for the Properties of Neutron Star Matter*, *ApJL* **887** (2019) L24.
- [8] V. Friese, *The cbm experiment at gsi/fair*, *Nuclear Physics A* **774** (2006) 377.
- [9] L. Lindblom, *Determining the nuclear equation of state from neutron-star masses and radii*, *The Astrophysical Journal* **398** (1992) 569.
- [10] R.C. Tolman, *Static solutions of einstein's field equations for spheres of fluid*, *Phys. Rev.* **55** (1939) 364.
- [11] J.R. Oppenheimer and G.M. Volkoff, *On massive neutron cores*, *Phys. Rev.* **55** (1939) 374.
- [12] G. Baym, C. Pethick and P. Sutherland, *The Ground State of Matter at High Densities: Equation of State and Stellar Models*, *APJ* **170** (1971) 299.
- [13] A.W. Steiner, M. Hempel and T. Fischer, *CORE-COLLAPSE SUPERNOVA EQUATIONS OF STATE BASED ON NEUTRON STAR OBSERVATIONS*, *The Astrophysical Journal* **774** (2013) 17.
- [14] A. Motornenko, J. Steinheimer, V. Vovchenko, S. Schramm and H. Stoecker, *Equation of state for hot qcd and compact stars from a mean-field approach*, *Phys. Rev. C* **101** (2020) 034904.
- [15] M. Alford, M. Braby, M. Paris and S. Reddy, *Hybrid stars that masquerade as neutron stars*, *The Astrophysical Journal* **629** (2005) 969.
- [16] D. Blaschke et al., *Astrophysics Constraints on the EOS*, in *Proceedings of 8th International Workshop on Critical Point and Onset of Deconfinement — PoS(CPOD 2013)*, vol. 185, p. 063, 2013, DOI.
- [17] S. Balberg and A. Gal, *An effective equation of state for dense matter with strangeness*, *Nuclear Physics A* **625** (1997) 435.
- [18] S. Banik, M. Hempel and D. Bandyopadhyay, *NEW HYPERON EQUATIONS OF STATE FOR SUPERNOVAE AND NEUTRON STARS IN DENSITY-DEPENDENT HADRON FIELD THEORY*, *The Astrophysical Journal Supplement Series* **214** (2014) 22.
- [19] T. Malik, S. Banik and D. Bandyopadhyay, *Equation-of-state table with hyperon and antikaon for supernova and neutron star merger*, *The Astrophysical Journal* **910** (2021) 96.
- [20] J.M. Lattimer and M. Prakash, *Neutron star structure and the equation of state*, *The Astrophysical Journal* **550** (2001) 426.
- [21] L. Rezzolla, E.R. Most and L.R. Weih, *Using gravitational-wave observations and quasi-universal relations to constrain the maximum mass of neutron stars*, *The Astrophysical Journal* **852** (2018) L25.

- [22] M. Shibata, E. Zhou, K. Kiuchi and S. Fujibayashi, *Constraint on the maximum mass of neutron stars using gw170817 event*, *Phys. Rev. D* **100** (2019) 023015.
- [23] E.R. Most, L.R. Weih, L. Rezzolla and J. Schaffner-Bielich, *New constraints on radii and tidal deformabilities of neutron stars from gw170817*, *Phys. Rev. Lett.* **120** (2018) 261103.
- [24] S. Soma and D. Bandyopadhyay, *Properties of binary components and remnant in GW170817 using equations of state in finite temperature field theory models*, *The Astrophysical Journal* **890** (2020) 139.
- [25] J.S. Read, B.D. Lackey, B.J. Owen and J.L. Friedman, *Constraints on a phenomenologically parametrized neutron-star equation of state*, *Phys. Rev. D* **79** (2009) 124032.
- [26] C.A. Raithel, F. Özel and D. Psaltis, *FROM NEUTRON STAR OBSERVABLES TO THE EQUATION OF STATE. I. AN OPTIMAL PARAMETRIZATION*, *ApJ* **831** (2016) 44.
- [27] L. Lindblom, *Spectral representations of neutron-star equations of state*, *Phys. Rev. D* **82** (2010) 103011.
- [28] M.-Z. Han, J.-L. Jiang, S.-P. Tang and Y.-Z. Fan, *Bayesian Nonparametric Inference of the Neutron Star Equation of State via a Neural Network*, *Astrophys. J.* **919** (2021) 11 [2103.05408].
- [29] I. Legred, K. Chatziioannou, R. Essick and P. Landry, *Implicit correlations within phenomenological parametric models of the neutron star equation of state*, 2022.
- [30] A.W. Steiner, J.M. Lattimer and E.F. Brown, *THE EQUATION OF STATE FROM OBSERVED MASSES AND RADII OF NEUTRON STARS*, *The Astrophysical Journal* **722** (2010) 33.
- [31] C.A. Raithel, F. Özel and D. Psaltis, *From Neutron Star Observables to the Equation of State. II. Bayesian Inference of Equation of State Pressures*, *ApJ* **844** (2017) 156.
- [32] S. Traversi, P. Char and G. Pagliara, *Bayesian inference of dense matter equation of state within relativistic mean field models using astrophysical measurements*, *The Astrophysical Journal* **897** (2020) 165.
- [33] Y. Fujimoto, K. Fukushima and K. Murase, *Methodology study of machine learning for the neutron star equation of state*, *Phys. Rev. D* **98** (2018) 023019.
- [34] Y. Fujimoto, K. Fukushima and K. Murase, *Mapping neutron star data to the equation of state using the deep neural network*, *Phys. Rev. D* **101** (2020) 054016.
- [35] Y. Fujimoto, K. Fukushima and K. Murase, *Extensive studies of the neutron star equation of state from the deep learning inference with the observational data augmentation*, *J. High Energy Phys.* **2021** (2021) 273.
- [36] F. Morawski and M. Bejger, *Neural network reconstruction of the dense matter equation of state derived from the parameters of neutron stars*, *A&A* **642** (2020) A78 [2006.07194].
- [37] M. Ferreira and C. Providência, *Unveiling the nuclear matter EoS from neutron star properties: a supervised machine learning approach*, *Journal of Cosmology and Astroparticle Physics* **2021** (2021) 011.
- [38] P.G. Krastev, *Translating Neutron Star Observations to Nuclear Symmetry Energy via Deep Neural Networks*, *Galaxies* **10** (2022) 16 [2112.04089].
- [39] S. Forte, L.s. Garrido, J.I. Latorre and A. Piccione, *Neural network parametrization of deep-inelastic structure functions*, *Journal of High Energy Physics* **2002** (2002) 062–062.
- [40] T.N. Collaboration, L.D. Debbio, S. Forte, J.I. Latorre, A. Piccione and J. Rojo, *Neural network determination of parton distributions: the nonsinglet case*, *Journal of High Energy Physics* **2007** (2007) 039–039.

- [41] L. Kades, J.M. Pawłowski, A. Rothkopf, M. Scherzer, J.M. Urban, S.J. Wetzel et al., *Spectral Reconstruction with Deep Neural Networks*, *Phys. Rev. D* **102** (2020) 096001 [[1905.04305](#)].
- [42] M. Zhou, F. Gao, J. Chao, Y.-X. Liu and H. Song, *Application of radial basis functions neural networks in spectral functions*, *Phys. Rev. D* **104** (2021) 076011 [[2106.08168](#)].
- [43] S.Y. Chen, H.T. Ding, F.Y. Liu, G. Papp and C.B. Yang, *Machine learning spectral functions in lattice QCD*, [2110.13521](#).
- [44] J. Carrasquilla and R.G. Melko, *Machine learning phases of matter*, *Nature Physics* **13** (2017) 431–434.
- [45] L.-G. Pang, K. Zhou, N. Su, H. Petersen, H. Stöcker and X.-N. Wang, *An equation-of-state-meter of quantum chromodynamics transition from deep learning*, *Nature Commun.* **9** (2018) 210 [[1612.04262](#)].
- [46] L. Wang, Y. Jiang, L. He and K. Zhou, *Continuous-mixture Autoregressive Networks for efficient variational calculation of many-body systems*, [2005.04857](#).
- [47] Y.-L. Du, K. Zhou, J. Steinheimer, L.-G. Pang, A. Motornenko, H.-S. Zong et al., *Identifying the nature of the QCD transition in relativistic collision of heavy nuclei with deep learning*, *Eur. Phys. J. C* **80** (2020) 516 [[1910.11530](#)].
- [48] R. Wang, Y.-G. Ma, R. Wada, L.-W. Chen, W.-B. He, H.-L. Liu et al., *Nuclear liquid-gas phase transition with machine learning*, *Phys. Rev. Res.* **2** (2020) 043202 [[2010.15043](#)].
- [49] L. Jiang, L. Wang and K. Zhou, *Deep learning stochastic processes with QCD phase transition*, *Phys. Rev. D* **103** (2021) 116023 [[2103.04090](#)].
- [50] D. Boyda, G. Kanwar, S. Racanière, D.J. Rezende, M.S. Albergo, K. Cranmer et al., *Sampling using  $SU(N)$  gauge equivariant flows*, *Phys. Rev. D* **103** (2021) 074504 [[2008.05456](#)].
- [51] K. Zhou, G. Endrődi, L.-G. Pang and H. Stöcker, *Regressive and generative neural networks for scalar field theory*, *Phys. Rev. D* **100** (2019) 011501 [[1810.12879](#)].
- [52] G. Kanwar, M.S. Albergo, D. Boyda, K. Cranmer, D.C. Hackett, S. Racanière et al., *Equivariant flow-based sampling for lattice gauge theory*, *Phys. Rev. Lett.* **125** (2020) 121601 [[2003.06413](#)].
- [53] M.S. Albergo, G. Kanwar and P.E. Shanahan, *Flow-based generative models for Markov chain Monte Carlo in lattice field theory*, *Phys. Rev. D* **100** (2019) 034515 [[1904.12072](#)].
- [54] M. Omana Kuttan, J. Steinheimer, K. Zhou, A. Redelbach and H. Stoecker, *A fast centrality-meter for heavy-ion collisions at the CBM experiment*, *Phys. Lett. B* **811** (2020) 135872 [[2009.01584](#)].
- [55] P. Thaprasop, K. Zhou, J. Steinheimer and C. Herold, *Unsupervised Outlier Detection in Heavy-Ion Collisions*, *Phys. Scripta* **96** (2021) 064003 [[2007.15830](#)].
- [56] F. Li, Y. Wang, H. Lü, P. Li, Q. Li and F. Liu, *Application of artificial intelligence in the determination of impact parameter in heavy-ion collisions at intermediate energies*, *J. Phys. G* **47** (2020) 115104 [[2008.11540](#)].
- [57] A. Andreassen, S.-C. Hsu, B. Nachman, N. Suaysom and A. Suresh, *Parameter estimation using neural networks in the presence of detector effects*, *Phys. Rev. D* **103** (2021) 036001 [[2010.03569](#)].
- [58] M.O. Kuttan, K. Zhou, J. Steinheimer, A. Redelbach and H. Stoecker, *An equation-of-state-meter for CBM using PointNet*, *JHEP* **21** (2020) 184 [[2107.05590](#)].
- [59] H. Huang, B. Xiao, Z. Liu, Z. Wu, Y. Mu and H. Song, *Applications of deep learning to relativistic hydrodynamics*, *Phys. Rev. Res.* **3** (2021) 023256 [[1801.03334](#)].

- [60] J. Peurifoy, Y. Shen, L. Jing, Y. Yang, F. Cano-Renteria, B.G. DeLacy et al., *Nanophotonic particle simulation and inverse design using artificial neural networks*, *Science Advances* **4** (2018) eaar4206 [<https://www.science.org/doi/pdf/10.1126/sciadv.aar4206>].
- [61] S. Shi, K. Zhou, J. Zhao, S. Mukherjee and P. Zhuang, *Heavy Quark Potential in QGP: DNN meets LQCD*, 2021.
- [62] L. Wang, S. Shi and K. Zhou, *Reconstructing spectral functions via automatic differentiation*, 2021.
- [63] I. Goodfellow, Y. Bengio and A. Courville, *Deep Learning*, MIT Press (Nov., 2016).
- [64] F. Chollet et al., “Keras.” <https://github.com/fchollet/keras>, 2015.
- [65] M. Abadi, A. Agarwal, P. Barham et al., *TensorFlow: Large-scale machine learning on heterogeneous systems*, 2015.
- [66] F. Douchin and P. Haensel, *A unified equation of state of dense matter and neutron star structure*, *A&A* **380** (2001) 151.
- [67] V. Pandharipande and R. Smith, *A model neutron solid with  $\pi^0$  condensate*, *Nuclear Physics A* **237** (1975) 507.
- [68] S. Typel, G. Röpke, T. Klähn, D. Blaschke and H.H. Wolter, *Composition and thermodynamics of nuclear matter with light clusters*, *Phys. Rev. C* **81** (2010) 015803.
- [69] F. Özel and D. Psaltis, *Reconstructing the neutron-star equation of state from astrophysical measurements*, *Phys. Rev. D* **80** (2009) 103003.
- [70] P.B. Demorest, T. Pennucci, S.M. Ransom, M.S.E. Roberts and J.W.T. Hessels, *A two-solar-mass neutron star measured using Shapiro delay*, *Nature* **467** (2010) 1081–1083.
- [71] K. He, X. Zhang, S. Ren and J. Sun, *Delving deep into rectifiers: Surpassing human-level performance on imagenet classification*, in *Proceedings of the IEEE international conference on computer vision*, pp. 1026–1034, 2015.
- [72] D.P. Kingma and J. Ba, *Adam: A method for stochastic optimization*, in *3rd International Conference on Learning Representations, ICLR 2015, San Diego, CA, USA, May 7-9, 2015, Conference Track Proceedings*, Y. Bengio and Y. LeCun, eds., 2015, <http://arxiv.org/abs/1412.6980>.
- [73] E.R. Most, L.J. Papenfort, V. Dexheimer, M. Hanauske, S. Schramm, H. Stöcker et al., *Signatures of quark-hadron phase transitions in general-relativistic neutron-star mergers*, *Phys. Rev. Lett.* **122** (2019) 061101 [[1807.03684](https://arxiv.org/abs/1807.03684)].
- [74] A. Figura, J.-J. Lu, G.F. Burgio, Z.-H. Li and H.-J. Schulze, *Hybrid equation of state approach in binary neutron-star merger simulations*, *Phys. Rev. D* **102** (2020) 043006.
- [75] D.P. Kingma and J. Ba, *Adam: A method for stochastic optimization*, 2017.
- [76] M. Nielsen, *Neural Networks and Deep Learning*, Determination Press, London (2015).
- [77] S. Hochreiter and J. Schmidhuber, *Long short-term memory*, *Neural Comput.* **9** (1997) 1735–1780.
- [78] X. Glorot and Y. Bengio, *Understanding the difficulty of training deep feedforward neural networks*, in *Proceedings of the thirteenth international conference on artificial intelligence and statistics*, pp. 249–256, JMLR Workshop and Conference Proceedings, 2010.
- [79] M. Holschneider, R. Kronland-Martinet, J. Morlet and P. Tchamitchian, *A real-time algorithm for signal analysis with the help of the wavelet transform*, in *Wavelets*, J.-M. Combes, A. Grossmann and P. Tchamitchian, eds., (Berlin, Heidelberg), pp. 286–297, Springer Berlin Heidelberg, 1990.



## A TOV-Solver Network

In order to train **TOV-Solver Network**, 52,000 EoS samples are taken from each set of polytropic EoSs. This accounts to 156,000 training samples corresponding to the three sets of EoSs for lower density region, which are shuffled before training. The hyperparameters of the network are initially modulated to acquire a working model. The network weights are tuned during the training process to reduce the mean squared error (MSE) between the output and the true M-R curve, which serves as the loss function for this regression task. The MSE is averaged over both the mass and radius with equal weights. Accuracy of the model is quantified by the coefficient of determination,  $\mathcal{R}^2$ , which is defined as  $1 - \frac{\sum_i (y_i - \hat{y}_i)^2}{(\sum_i (y_i - \bar{y})^2 + \delta)}$ . Here,  $y_i$  is the true value of the  $i^{\text{th}}$  M-R pair,  $\hat{y}_i$  is the corresponding prediction from the network, and  $\bar{y}$  is the mean of the true M-R values. We set  $\delta = 10^{-7}$  to avoid undefined values when encountered with a division by zero. Once the loss converges, the weights are finalized and we are left with a well-functioning generic model. The remaining 72,569 EoS samples, exclusive of the training set, are then used for the validation and testing of the network.

Illustrated in the sections below are detailed versions of four unique types of DL models that were constructed, trained and then tested to perform this task. The input and output layers of the networks are of the same length. The dimensions, however, are different. The input layer has one channel, corresponding to the pressure  $P(\rho)$ , and the output layer contains two channels for the M-R pairs. Each type of model was built with two different resolutions for the data-set, i.e,  $N_\rho = 128$  and 32; resulting in eight distinct models. We used the Adam optimizer [75], with learning rate,  $\alpha = 0.0003$  for all the models. They were all trained by minimizing the loss function, MSE, in batches of size 4096. The accuracy of all the models was estimated by the  $\mathcal{R}^2$  metric, and reaches around 99.9% in each case. Further specifics are mentioned in their respective modules below, and a comparison of the models' functioning is done towards the end of Appendix A.

### A.1 Fully Connected Dense Neural Network (FCN)

A fully connected dense neural network is a feed-forward network with fully connected layers, meaning that every single neuron in a layer (hidden or output) is connected to the preceding layer's neurons. The models pertaining to our task have the architectures as portrayed in Table 1 for both  $N_\rho = 128$  and 32. In both cases, the ELU activation function was applied on the hidden layers, and Sigmoid on the output layer. The model weights were initialized with the *He* Normal distribution [71]. An  $L_2$  regularization penalty ( $\lambda = 10^{-7}$ ) was applied on the layer weights. The FCN models were trained for 15,000 epochs, given their significantly superior training times when compared to the rest of the DL models. Further details of performance are given in Table 5.

### A.2 Convolutional Neural Network (CNN)

CNNs are widely used as they have the potential to extract key features or patterns in the input data. This type of a DL model is explored to make certain the network is not rendered obsolete when encountered with stark changes in the pressure gradient. The CNN consists of a convolutional kernel or matrix for each layer, which is used to compute the outputs of the succeeding layer [76]. The number of layers in the two CNN models that we built and their dimensions are listed in Table 2. A kernel size of  $3 \times 1$  is used for both the models, with the weights initialized from the *He* Normal distribution [71], and penalized with the  $L_2$  regularizer

**Table 1.** The FCN model architecture used for the TOV-Solver Network.

Layer Index	Layer	Dimension	
		$N_\rho = 128$	$N_\rho = 32$
Input	-	128	32
1	Dense	128	32
2	Dense	64	64
3	Dense	32	128
4	Dense	64	64
-	Add (2,4)	64	64
5	Dense	128	32
-	Add (1,5)	128	32
6	Dense	256	64
Output	Reshape	(128,2)	(32,2)

( $\lambda = 10^{-6}$ ). Stride values of 1 and 2 are applied alternatively on the convolutional layers. We employ the ELU activation function on the hidden layers and Sigmoid on the output layer. The padding ‘*same*’ is applied to the convolutional layers to disallow loss of information at the boundaries or a change in dimension of the following layer.

**Table 2.** The CNN model architecture used for the TOV-Solver Network.

Layer Index	Layer	Dimension	
		$N_\rho = 128$	$N_\rho = 32$
Input	-	(128,1)	(32,1)
1	Convolution 1D	(128,128)	(32,32)
2	Convolution 1D	(64,64)	(16,64)
3	Convolution 1D	(64,64)	(16,64)
-	Add (2,3)	(64,64)	(16,64)
4	Convolution 1D	(32,64)	(8,64)
5	Convolution 1D	(32,64)	(8,64)
-	Add (4,5)	(32,64)	(8,64)
6	Convolution 1D	(16,32)	(4,32)
7	Convolution 1D	(16,32)	(4,32)
-	Add (6,7)	(16,32)	(4,32)
-	Reshape	512	128
8	Dense	128	32
9	Dense	256	64
Output	Reshape	(128,2)	(32,2)



### A.3 Long Short Term Memory (LSTM) Network

The Long Short Term Memory, or LSTM, is a recurrent NN, which as the name suggests, has recurrent connections or feedback loops in a layer, in order to retain memory in a sequence [77]. The recurring units or memory cells in LSTM carry the dependency across time sequences, leading to longer training times (see Table 5 for a comparison to other models). Due to the fact that the output layer is an M-R sequence, the prospects of LSTM for the **TOV-Solver Network** are examined. The model descriptions are given in Table 3 for  $N_\rho = 128, 32$ . The kernel parameters of all the layers were initialized from the Xavier or Glorot uniform distribution [78], and the  $L_2$  regularization ( $\lambda = 10^{-7}$ ) was applied. In this case, we used the Tanh activation function for the LSTM layers.

**Table 3.** The LSTM model architecture used for the TOV-Solver Network.

Layer Index	Layer	Dimension	
		$N_\rho = 128$	$N_\rho = 32$
Input	-	(128,1)	(32,1)
1	LSTM	(128,128)	(32,32)
2	LSTM	(128,64)	(32,64)
3	LSTM	(128,128)	(32,64)
4	LSTM	(128,128)	(32,32)
-	Add (1,4)	(128,128)	(32,32)
5 (Output)	LSTM	(128,2)	(32,2)

### A.4 WaveNet

The WaveNet is a generative NN model with autoregressive properties. The network is structured with convolutional layers that make use of dilated kernels [79]. The hidden layers with inflated kernels along with ‘causal’ padding ensure the autoregressive behaviour of the network, without forfeiting any information. The network mimics the concept of autoregression that is exercised in solving the TOV equations, and is therefore used in further stages of our research study. The kernel parameters are initialized from the Xavier or Glorot uniform distribution [78], and the  $L_2$  regularization ( $\lambda = 10^{-7}$ ) is applied. The ELU activation function is applied on the all the layers but the last (Sigmoid activation).

### A.5 Comparison

The performance of the different models was examined on a validation set, which is exclusive of the training data. The tables show that given EoSs, all the DNNs are capable of finding their TOV solutions at precisions that reach  $\mathcal{R}^2=99.9\%$ . The LSTM and WaveNet models are typically used for training series or sequences. Therefore, we observe a boost in their performances when combined with the **EoS-Network**.

## B Mock Tests on SFHo and BHBA $\phi$ EoSs.

Here, we show the performance of the neural networks on the reconstruction of SFHo and BHBA $\phi$  EoSs, using the proposed method. The mock M-R observational data points are

**Table 4.** The WaveNet model architecture used for the TOV-Solver Network.

Layer Index	Layer	Dilation	Dimension	
			$N_\rho = 128$	$N_\rho = 32$
Input	-	-	(128,1)	(32,1)
1	Convolution 1D	-	(128,128)	(32,32)
2	Convolution 1D	1	(128,128)	(32,32)
3	Convolution 1D	2	(128,128)	(32,32)
4	Convolution 1D	4	(128,128)	(32,32)
5	Convolution 1D	8	(128,128)	(32,32)
6	Convolution 1D	16	(128,128)	(32,32)
7	Convolution 1D	32	(128,128)	(32,32)
8	Convolution 1D	16	(128,128)	(32,32)
9	Convolution 1D	32	(128,128)	(32,32)
10 (Output)	Convolution 1D	64	(128,2)	(32,2)

**Table 5.** Comparison of the performance of different Neural Networks for solving the TOV equations.

$N_\rho$	NN	$\mathcal{R}^2$	MSE	Parameters	Epochs	Time
			( $\times 10^{-5}$ )	(#)	( $\times 10^3$ )	( $\times 10^3 sec$ )
128	CNN	0.9999	1.743	170,176	3.5	7.35
	FCN	0.9999	1.052	70,304	15	4.91
	LSTM	0.9998	0.741	347,416	3	32.5
	WaveNet	0.9998	3.003	296,706	3	64.7
32	CNN	0.9999	3.019	58,912	3.5	2.15
	FCN	0.9999	1.179	23,936	15	2.79
	LSTM	0.9999	0.814	74,904	3	4.03
	WaveNet	0.9999	3.047	18,882	3	10.7

taken from corresponding M-R curve obtained with the SFHo or BHBA $\phi$  EoSs. We perform the tests without assuming uncertainties. The reconstructed SFHo and BHBA $\phi$  EoSs obtained from the optimization procedure are depicted as red dashed curves in the left panels of Figure 11 and Figure 12 respectively. The results are compared with the true EoSs which are depicted as solid black curves. The M-R curves obtained from the reconstructed EoSs (red dashed curves) are also shown against the true M-R curves (solid black curves) in the right panels of Figure 11 and Figure 12.

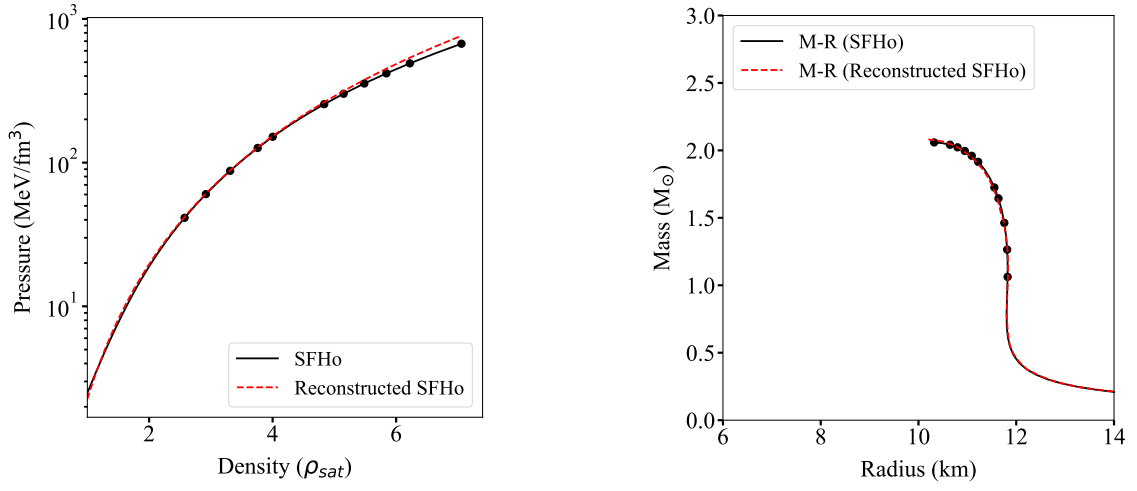


**Figure 11.** Reconstruction performance check on the SFHo EoS.

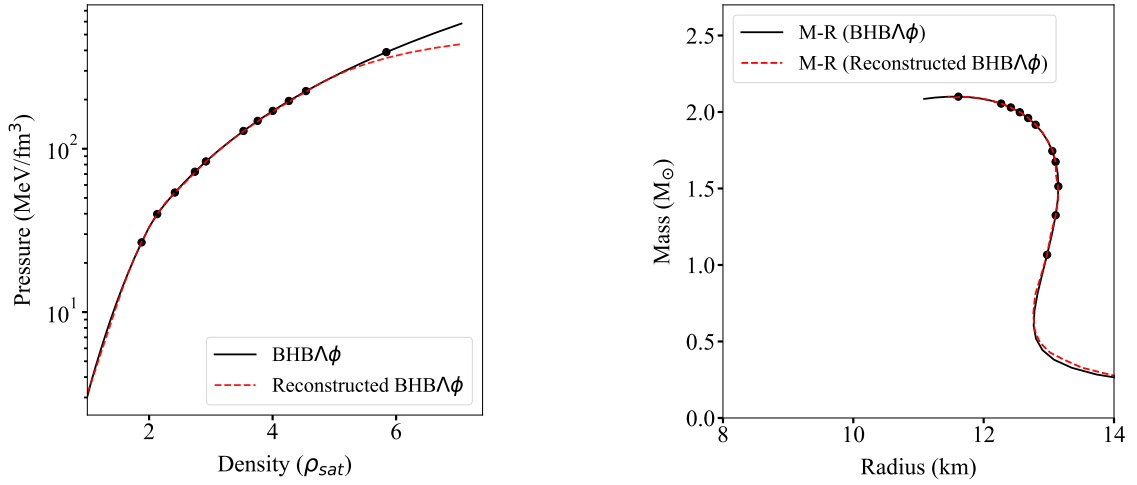


**Figure 12.** Reconstruction performance check on the BHBA $\phi$  EoS.